IMAGE & SIGNAL PROCESSING

Combination of Enhanced Depth Imaging Optical Coherence Tomography and Fundus Images for Glaucoma Screening

Zailiang Chen[1] · Xianxian Zheng[1] · Hailan Shen[1] ⊙ · Ziyang Zeng[1] · Qing Liu[1] · Zhuo Li[2]

Abstract

Glaucoma is an eye disease that damages the optic nerve and can lead to irreversible loss of peripheral vision gradually and even blindness without treatment. Thus, diagnosing glaucoma in the early stage is essential for treatment. In this paper, an automatic method for early glaucoma screening is proposed. The proposed method combines structural parameters and textural features extracted from enhanced depth imaging optical coherence tomography (EDI-OCT) images and fundus images. The method first segments anterior the lamina cribrosa surface (ALCS) based on region-aware strategy and residual U-Net and then extracts structural features of the lamina cribrosa, such as lamina cribrosa depth and deformation of lamina cribrosa. In fundus images, scanning lines based on disc center and brightness reduction are used for optic disc segmentation and brightness compensation is utilized for segmenting the optic cup. Afterward, the cup-to-disc ratio (CDR) and textural features are extracted from fundus images. Hybrid features are used for training and classification to screen glaucoma by gcForest in the early stage. The proposed method has given exceptional results with 96.88% accuracy and 91.67% sensitivity.

Keywords Glaucoma screening · EDI-OCT · Fundus images · Hybrid feature extraction

Introduction

Glaucoma is the world's second most common blinding disease and most common irreversible blinding disease worldwide [1–3]. It is expected that there are 79 million glaucoma patients in the world in 2020 [4]. Glaucoma damages the optic nerve, causes loss of peripheral vision and leads to irreversible loss of vision. While vision filed tests are clinical techniques, imaging modalities such as spectral domain optical coherence tomography and stereoscopic fundus photography are also useful for glaucoma screening. Recent developing optical coherence tomography (OCT) technology have been applied in many eye diseases [5, 6]. Anterior lamina cribrosa surface

depth (ALCSD) and other structural parameters, which are characteristics of glaucoma and change over the process, can be obtained from OCT and fundus images. For example, Fig. 1 shows ALCSD, which is defined as the distance between Bruch's membrane opening (BMO) baseline and anterior lamina cribrosa surface (ALCS). Elevated intraocular pressure is associated directly with the optic nerve injury and can lead to posterior sliding and bowing of lamina cribrosa [7]. Thus, ALCSD is larger in glaucoma than in normal eyes.

Lamina cribrosa can be seen clearly in anterior segment enhanced depth imaging optical coherence tomography (EDI-OCT) after removing retina and part of the prelamina tissue [8]. Recent cross-sectional studies [9–12] shows that lamina cribrosa is a new biomarker for glaucoma screening. Focal lamina cribrosa defects [9], lamina cribrosa thickness [10], and lamina cribrosa depth [11, 12] are related to glaucoma and these structural parameters are significantly different between glaucoma and normal eyes. Automatic lamina cribrosa detection algorithms have been developed [13, 14]. The method in [13] uses active contour and energy constraints to measure lamina cribrosa depth. Belghith et al. [14] use non-local energy function in Markov random field to improve segmentation results. Our proposed novel algorithm of lamina

✉ Hailan Shen
  hn_shl@126.com

1 School of Computer Science and Engineering, Central South University, Changsha 410083, China

2 The Second Xiangya Hospital of Central South University, Changsha 410011, China
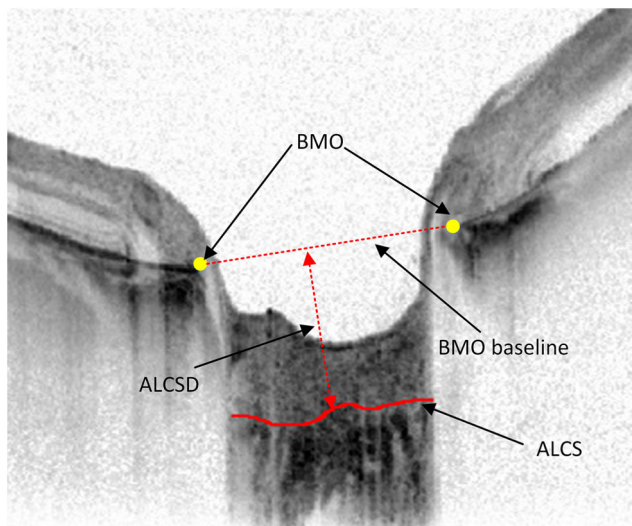
Fig. 1 Anterior lamina cribrosa surface depth

cribrosa segmentation in this paper is based on region-aware strategy and residual U-Net and obtains better segmentation results.

Currently, researchers develop their studies for glaucoma screening mainly on fundus images [15–22] and OCT [23, 24]. Haleem et al. [15] propose a novel adaptive deformable model for automated optic disc and cup segmentation to aid glaucoma diagnosis. The approach of Noronha et al. [16] uses high order cumulant features extracted from fundus images and classify fundus images into four groups: normal, mild glaucoma, moderate glaucoma, and severe glaucoma. Khalil et al. [17] combine structural parameters and textural features for classification. Structural parameters and textural features are trained by support vector machine and outputs are of three classes, such as normal, glaucoma and suspected glaucoma. In [18], an adaptive threshold method is proposed for segmenting the optic disc and cup. The cup-to-disc ratio (CDR), rim area, and vessel information are extracted from fundus images for glaucoma screening. In the work of Maheshwari et al. [19], empirical wavelet transform (EWT) and correntropy are applied to extract features and least-square support vector machine (LS-SVM) is used for classifying glaucoma. Soltani et al. [20] use fuzzy logic and image processing for glaucoma screening. In view of the fact that retinal ganglion cell axons pass through the optic cup to leave eyes, blood vessel tracking and bend point detection are used to detect edge pixels of cup and CDR is calculated for predicting glaucoma [21]. Deep neural network framework which has eighteen layers has been utilized for diagnosing glaucoma using fundus images [22].

While the aforementioned approaches use fundus images for classification, Niwas et al. [23] use anterior segment OCT to extract compound image transform features and naive Bayes classifier is used for classification. Inspired by recent medical studies, Gopinath et al. [24] extract blood vessel density and retinal nerve fiber layer depth from Angio-OCT and support vector machine has been used to divide images into glaucoma group or normal group afterward.

The existing approaches for glaucoma screening mainly use fundus images while a few of them use OCT. Nevertheless, these methods use features extracted from only one kind of image, and the performances of these methods are limited to the information provided by one kind of image. Different kinds of ophthalmic images involve information of pathology from different angles. We can acquire information about retinal layers and optic nerve injury from EDI-OCT, while fundus images provide more detailed texture changes. To the best of our knowledge, no related work has yet combined features extracted from EDI-OCT and fundus images for glaucoma screening.

The purpose of our work is to develop a novel method that utilizes information both from EDI-OCT images and fundus images to screen glaucoma in the early stage. The proposed novel method combines structural parameters and textural features in EDI-OCT images and fundus images. In OCT images, we use region-aware strategy and residual U-Net to compute the possibility of each pixel in the whole image belonging to either ALCS or background. Pixels with high possibility are chosen to obtain precise ALCS. After segmenting ALCS, structural parameters such as lamina cribrosa depth and Bruch's membrane opening-minimum rim width (BMO-MRW) are extracted. In fundus images, our approach segments the optic disc using scanning lines based on contour center and detects the optic cup using brightness compensation. CDR and textural features are extracted from fundus images. The gcForest [25] is trained by the aforementioned features and the approach has given superior results with 96.88% accuracy and 91.67% sensitivity. And the contributions of this paper are shown as follows:

1) The combination of structural parameters and textural features extracted from EDI-OCT images and fundus images is used for the first time to screen glaucoma. It is a new attempt to help ophthalmologists diagnose glaucoma in the early stage.
2) We propose a method for anterior lamina cribrosa segmentation in EDI-OCT based on region-aware strategy and residual U-Net.
3) An improved templated local binary pattern (TLBP) is used to extract features of lamina cribrosa deformation.

The proposed method

In this section, we present our novel method for screening glaucoma in EDI-OCT and fundus images. The purpose of this study is to detect anterior lamina cribrosa surface in

EDI-OCT and segment the optic disc and cup region, then extract the hybrid features based on prior clinical knowledge, and then classify the multimodal images into normal group or glaucoma group. The flowchart presented in Fig. 2 shows the steps of the proposed method.

Anterior lamina cribrosa surface segmentation

We present an ALCS segmentation algorithm based on region-aware strategy and U-Net [26]. A single pixel of ALCS in A-scan (one column in B-scan) is not easy to detect using only information of A-scan. Nevertheless, features from neighbor pixels are useful for detecting ALCS pixels. Inspired by this, we transform the problem of detecting a single line into the problem of region segmentation. Particularly, pixels that are less than or equal to five pixels from labeled ALCS are considered as ALCS pixels in label images, and pixels that are more than five pixels from ALCS are considered as background. Thus, the surface line expands to a regional area. We use residual U-Net: a fully convolutional neural network based on the widely used U-Net, to segment expanded ALCS area. Residual U-Net takes advantages of U-Net skip connections [27] and residual learning skill [28] to obtain a robust segmentation result. The skip connections in U-Net capture both the local and contextual information [27, 28], while the residual connections allow a better flow of the gradient information through the network. Residual U-Net is trained with EDI-OCT images of the optic nerve head (ONH) and corresponding manually segmented ground truths. In each column

of the segmented region, the pixel with the highest probability belonging to ALCS is selected as the ALCS pixel.

Adaptive compensation

Adaptive compensation (AC) is used to remove the effects of light attenuation caused by imaging modality [29]. AC is useful for removing blood vessel shadows and enhance the contrast of OCT images of the ONH [30]. The contrast exponent is set to 4 for improving the overall image contrast and the threshold exponent is set to 6 for limiting noise over-amplification at the bottom of the compensated image. AC is used for all B-scans and we stack up B-scan and its compensated B-scan as input images of residual U-Net.

Network architecture

The residual U-Net architecture is composed of multi-scale residual blocks shown in Fig. 3. Residual blocks in the downsampling tower connect to the block with the same scale in the upsampling tower via skip connections. Skip connections concatenate feature maps in the downsampling tower and corresponding feature maps in the upsampling tower to acquire robust features for segmentation. In the downsampling tower, a B-scan of size 496×512 is fed to the first residual block with 32 convolution filters followed by three different scale residual blocks with the same number of convolution filters. A max-pooling is used for downsampling after every residual block. A residual block with 32 convolution filters in upsampling tower concatenates features from an additional
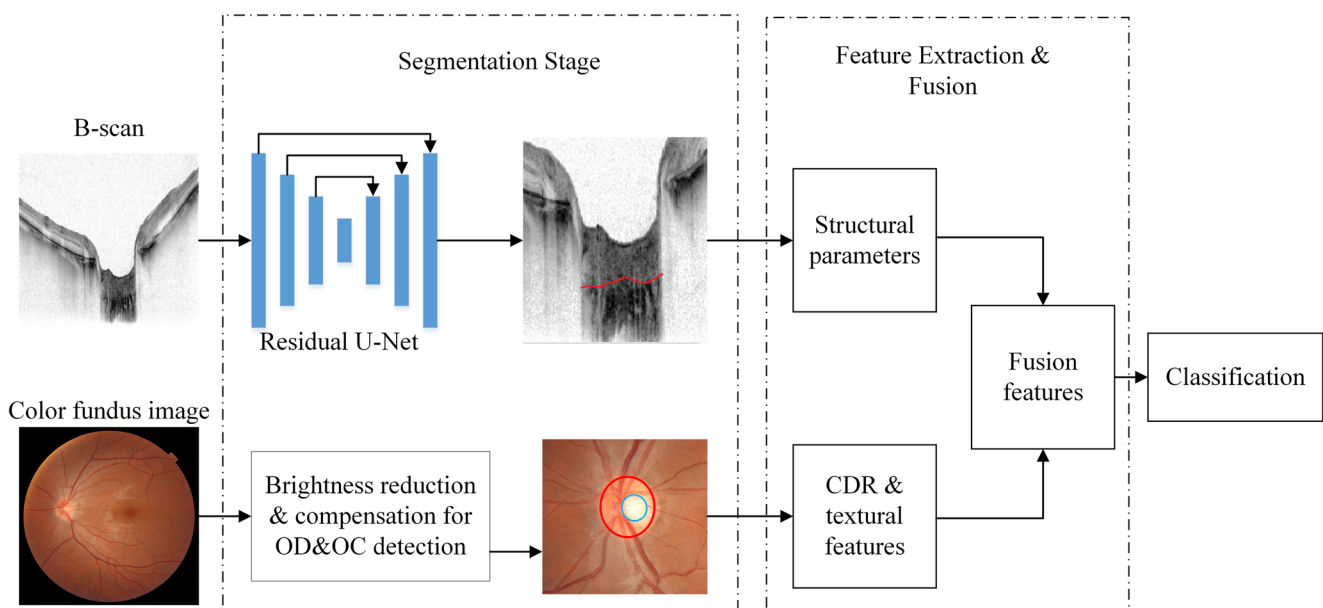

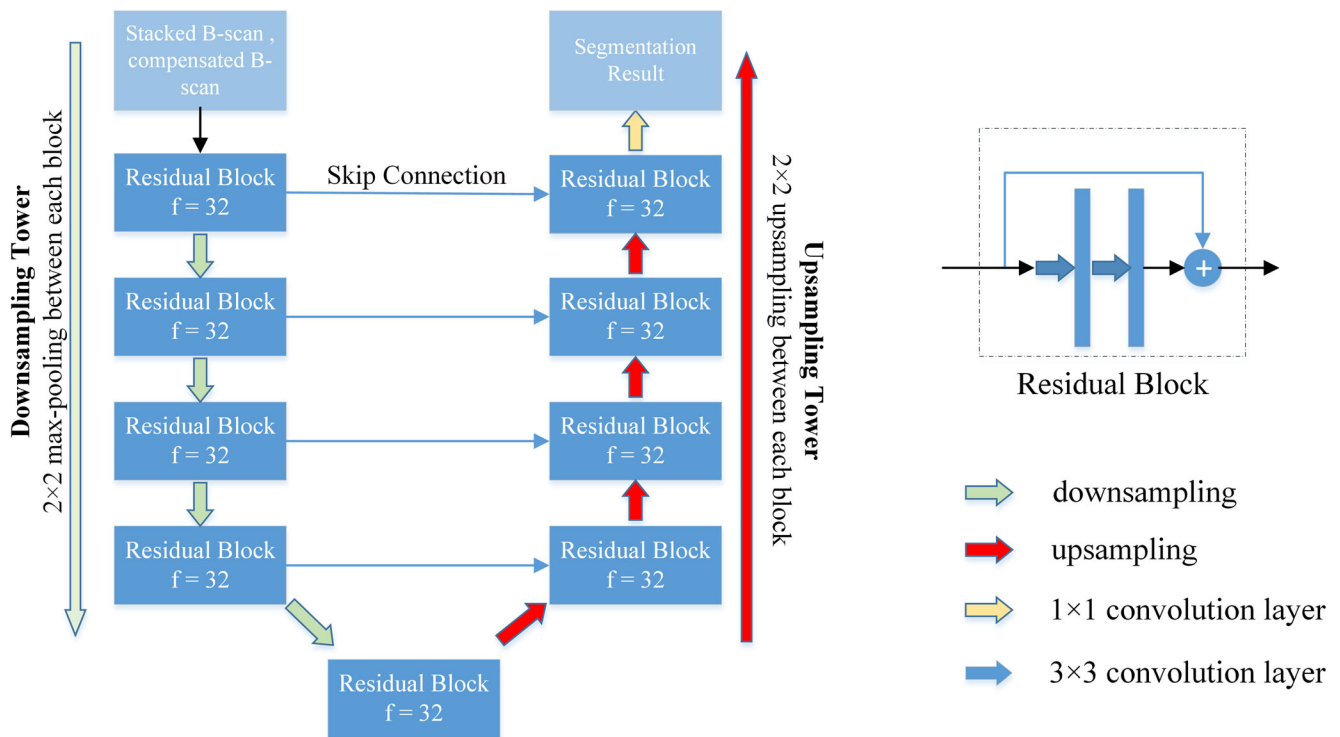**Fig. 2** The flowchart of the proposed method

Fig. 3 Residual U-Net architecture. Best viewed in color

residual block between two towers and the corresponding residual block with the same scale. Then features are fed to three residual blocks with different scales. An upsampling layer is used before every residual block. The output of the upsampling tower is fed to a 1×1 convolution layer with 1 filter. The sigmoid activation function is applied to obtain the probability for each pixel.

In two towers, all the layers except the output layer are activated by ReLU [31]. And the loss function is based on dice loss:

$$L\left(\hat{Y}, Y\right) = 1 - \frac{1}{m} \sum_{i=1}^{m} \frac{2|\hat{Y} \cap Y|}{|\hat{Y}| + |Y|}, \tag{1}$$

where m denotes the total number of samples, $\hat{Y}$ denotes the predicted value, and Y denotes the label.

Training and testing of network

We train our network with 46 OCT images and test it with 32 OCT images. In the training stage, data augmentation (random rotation, shearing, and horizontal flipping) is performed to overcome the sparsity of our training data and stochastic gradient descent with a momentum of 0.9 is used to optimize the training process. An initial learning rate of 0.001 is chosen and it is divided by 10 when the validation loss fails to improve. The model with the best validation loss is chosen to measure

test dataset. The pixel with the highest possibility in each column of each B-scan is chosen as the final ALCS pixel.

Optic disc segmentation

CDR is always significantly different between glaucoma and normal eyes in fundus images. Thus, CDR is used to improve the performance of glaucoma screening. A robust algorithm of disc segmentation based on contour center scanning line is proposed.

The optic disc is usually the brightest area in fundus images. The proposed algorithm first find the location of the optic disc using brightness reduction and shape constraint to remove pixels that do not belong to the optic disc. Scanning lines based on contour center are used for accurate segmentation of the optic disc.

The red channel is sensitive to brightness in color channels. In the red channel of fundus images, the brightness value of the optic disc is high and thus the edge of the optic disc is relatively clear. The brightness is reduced to remove the pixels that do not belong to the optic disc. The formula of brightness reduction is defined in formula (2).

$$I^k(i,j) = I^k(i,j) - \mu^{k-1} - \sigma^{k-1}, \tag{2}$$

where $I^k(i,j)$ is the pixel (i,j) in fundus images, and k represents the number of iterations. μ^{k-1} and σ^{k-1} represent the average brightness value of fundus image and standard

deviation of pixel brightness after k iterations. In an $m \times n$ matrix, μ and σ are given by

$$\mu^k = \frac{1}{mn} \sum_{i=1}^{m} \sum_{j=1}^{n} I^k(i,j), \tag{3}$$

$$\sigma^k = \sqrt{\frac{1}{mn} \sum_{i=1}^{m} \sum_{j=1}^{n} \left(I(i,j) - \mu^k \right)^2}. \tag{4}$$

The brightness reduction operation is carried out four times, and the corresponding four brightness reduction processing results of different degrees are obtained respectively. The brightness reduction operation is shown in Fig. 4.

After brightness reduction, some pixels that are highly similar to pixels of the optic disc still exist. Thus, we need to select an appropriate area in every image after brightness reduction. Shape constraints are used to select an appropriate area in each image. We select the largest area in each image, use ellipse-fitting method and calculate the ratio of major axis and minor axis of the fitted ellipse in selecting the appropriate the optic disc area, while considering some small noises and bright arcs in processed images and the main difference in the number of pixels and shape among those areas and the optic disc. The area selection suppresses noises and calculation of the ratio of major axis and minor axis is helpful for eliminating the effect of bright arcs caused by inappropriate light sources in the imaging process. The optic disc tends to have a low ratio of major axis and minor axis, while the bright arc has a high ratio. In all the four processed images, the area with the lowest ratio is considered as the optic disc area.

Since the location of the optic disc is located, the contour center, which is the geometric center of the optic disc area, can be determined. We intercept a 501×501 image block centered by the contour center and extract a scanning line every 10 degrees starting from the contour center in the image block. The two ends of the scanning line are the contour center pixel and edge pixel of the intercepted image block, and 36 lines are extracted from the image block. For each scanning line, the gray value of the corresponding pixel on the scanning line is extracted to form the curve of image gray value. The overall trend of the grayscale curve is gradually decreased and we use the sigmoid function to fit the curve after normalizing gray values. Pixels corresponding to the curve threshold of 0.9 and above are taken as the pixel points in the optic disc and the pixel corresponding to the threshold of 0.9 are candidate boundary points of the optic disc. Based on the polygon convex hull method, the accurate boundary of the optic disc is obtained.

Optic cup segmentation

In fundus images, the boundary of the optic cup is not obvious in some images. We use adaptive brightness compensation as

$$I(i,j) = \frac{\mu}{D} \cdot I(i,j), \tag{5}$$

where $I(i,j)$ represents the intensity of pixel (i,j), and μ is the median gray value of 11×11 image block center by pixel (i,j). D is the compensations factor used to suppress the gray value of pixels near the border in image block and compensate the gray value of center pixels and D is given by

$$D = 0.05 \sqrt{(i - x_c)^2 + (j - y_c)^2 + 1}, \tag{6}$$

where x_c and y_c are coordinates at the center of the region, and the constant 1 is set for ensuring that D is greater than zero. After compensation, a threshold is used to obtain the optic cup boundary. After the experiment, when the threshold value is 55, good results are shown in different images. Pixels higher than the threshold value are reserved as cup pixels, while those lower than the threshold value are taken as rim pixels (pixels between disc boundary and cup boundary).
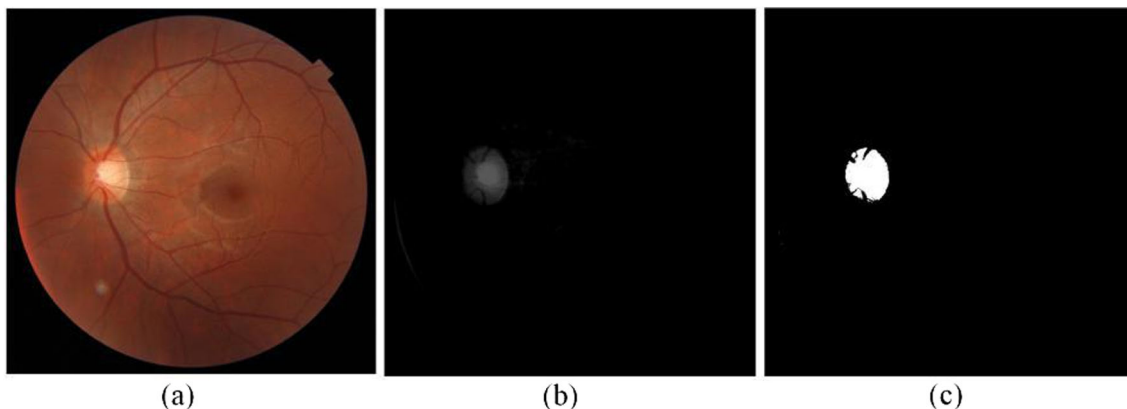

Fig. 4 Brightness reduction operation. (**a**) A fundus image, (**b**) after brightness reduction, (**c**) after threshold

Hybrid features extraction

Combining structural parameters extracted from EDI-OCT images and features extracted from color fundus images is a new attempt to screen glaucoma in the early stage. We extract features such as anterior lamina cribrosa depth, deformation of lamina cribrosa and BMO-MRW from EDI-OCT images, while CDR and textural features are extracted from fundus images.

Lamina cribrosa features extraction

Recent studies have shown that lamina cribrosa that can be seen clearly in EDI-OCT images is related to the pathogenesis of glaucoma and lamina cribrosa may become a new biomarker for diagnosing glaucoma [9–12]. In our proposed method, ALCSD and information of lamina cribrosa deformation are extracted.

ALCSD is defined as the distance between the ALCS and the BMO reference plane. ALCSD is more likely to be larger in glaucoma than in normal eyes because of posterior displacement. Minimum, maximum and average depths of ALCS are extracted.

Besides posterior displacement, lamina cribrosa deformation occurs in glaucoma eyes. Templated local binary pattern algorithm is used to extract information of lamina cribrosa deformation. ALCS pixels, upper pixels and lower pixels on the segmented ALCS are selected as the candidate pixels and their LBP [32] values are calculated. Four templates are used to reduce dimensions of the feature set considering that the extracted feature set contains useless textural information, such as textural information of lamina cribrosa holes and speckle noises produced in the imaging process of OCT images. Slope templates and horizontal templates are shown in Fig. 5. Figure 5 (a) and (b) are slope templates, whereas Fig. 5 (c) and (d) are horizontal templates. Slope templates describe the sharp changes of ALCS in grayscale and horizontal templates represent smoothness of ALCS.

For each LBP value, we calculate the distance D between LBP value and each template and select the LBP value if D is smaller than the constant 2. Distance D is defined as the number of different binary bits between computed LBP value and template. We divide the remaining LBP values into four groups by distance D. LBP value is considered to belong to the group if it has the shortest distance from the group. We count the number of LBP values corresponding four templates and calculate r_s and r_h using formulas as follows:

$$r_s = \frac{n_a + n_b}{n_a + n_b + n_c + n_d}, \tag{7}$$

$$r_h = \frac{n_c + n_d}{n_a + n_b + n_c + n_d}, \tag{8}$$

where n_a, n_b, n_c and n_d are numbers of LBP values corresponding to four templates respectively, and r_s and r_h are ratios of LBP values corresponding to slope templates and horizontal templates. r_s and r_h are extracted as features of lamina cribrosa deformation.

Bruch's membrane opening minimum rim width extraction

BMO-MRW is defined as the minimum distance from the BMO to the ILM. In glaucoma eyes, BMO-MRW is more likely to be small while it is relatively large in normal eyes [33]. Two values of BMO-MRW are extracted in each EDI-OCT B-scan. Figure 6 shows the illustration of BMO-MRW extraction.

Cup-to-disc ratio calculation

CDR is conventionally assessed by ophthalmologists in the screening and monitoring of glaucoma. Enlargement of the cup has been observed in glaucoma patients [34]. We extract vertical and horizontal CDR in fundus images. Illustrations of vertical CDR and horizontal CDR are depicted in Fig. 7.

Gray-level co-occurrence matrix features extraction

The gray-level co-occurrence matrix (GLCM) provides statistical information about the relative locations of the neighborhood pixels in images [35]. GLCM is used to extract textural features from fundus images and entropy, correlation, and

Fig. 5 Designed templates. (**a**), (**b**) Slope templates. (**c**), (**d**) Horizontal templates

1	0	0
1		0
1	1	1

(a)

1	1	1
0		1
0	0	1

(b)

0	0	0
0		0
1	1	1

(c)

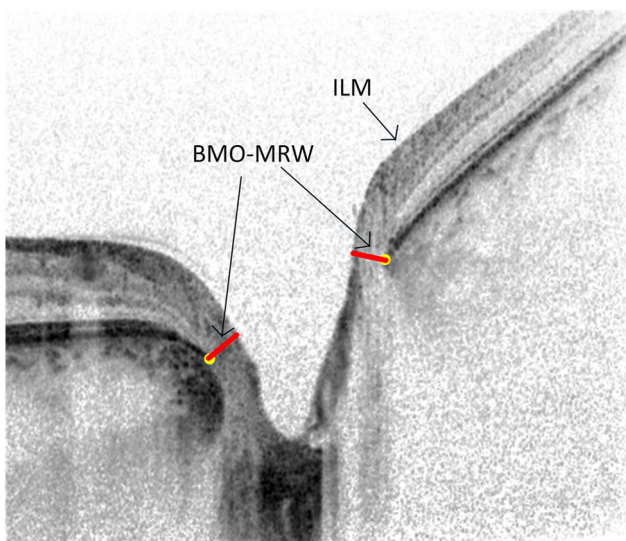| 1	1	1
0		0
0	0	0

(d)
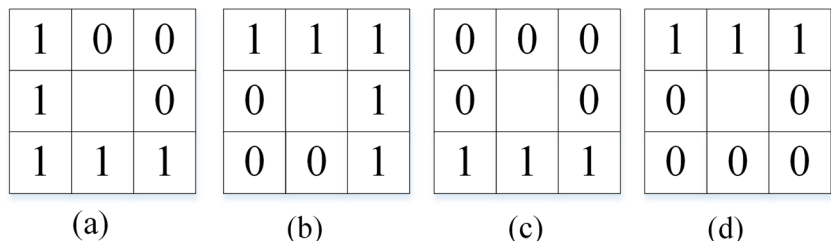
Fig. 6 The illustration of the BMO-MRW

homogeneity [36] are extracted and utilized in the proposed method.

Correntropy features extraction

Correntropy is a nonlinear kernel based measure of similarity which preserves both statistical and temporal information [37]. It measures correlation in nonlinear domain of multiple delayed samples of the signal. The features based on correntropy can be used to estimate the distribution of texture in decomposed image components. We use empirical wavelet transform [38] to decompose fundus images in red, green and blue channels. Every channel is decomposed into two

components and three correntropy features are extracted from each component. The correntropy for lag G is defined as

$$Correntropy(G) = \left(\frac{1}{X-G+1}\right)^2$$
$$\times \sum_{x_1,x_2=G}^{X} K(I[x_1,x_2]-I[x_1-G,x_2-G]), \quad (9)$$

where $I[x_1,x_2]$ is the 2-D signal, X is the number of rows and columns, and the Gaussian kernel function $K(I[(x_1,x_2)]-I[x_1-G,x_2-G])$ can be given by

$$K(I[x_1,x_2]-I[x_1-G,x_2-G]) = \frac{1}{\sqrt{2\pi\varepsilon}} \times \exp\left\{-\frac{(I[x_1,x_2]-I[x_1-G,x_2-G])^2}{2\varepsilon^2}\right\},$$
$$(10)$$

where ε is the kernel parameter width, and G controls the number of extracted features. In our experiment, we set $G = 3$, $\varepsilon = 3$, and the factor $\frac{1}{X-G+1}$ is considered as 1.

Glaucoma classification

In the proposed method, classification is performed on hybrid features extracted from EDI-OCT images and fundus images using gcForest as the classifier. The gcForest has excellent performance in small datasets and can be trained easily [25]. In our case, we used random forest and extra tree as individual learners. For each input eigenvector, gcForest predicts the possibilities of belonging to glaucoma eyes or normal eyes and chooses the class with the highest possibility as the result of classification.
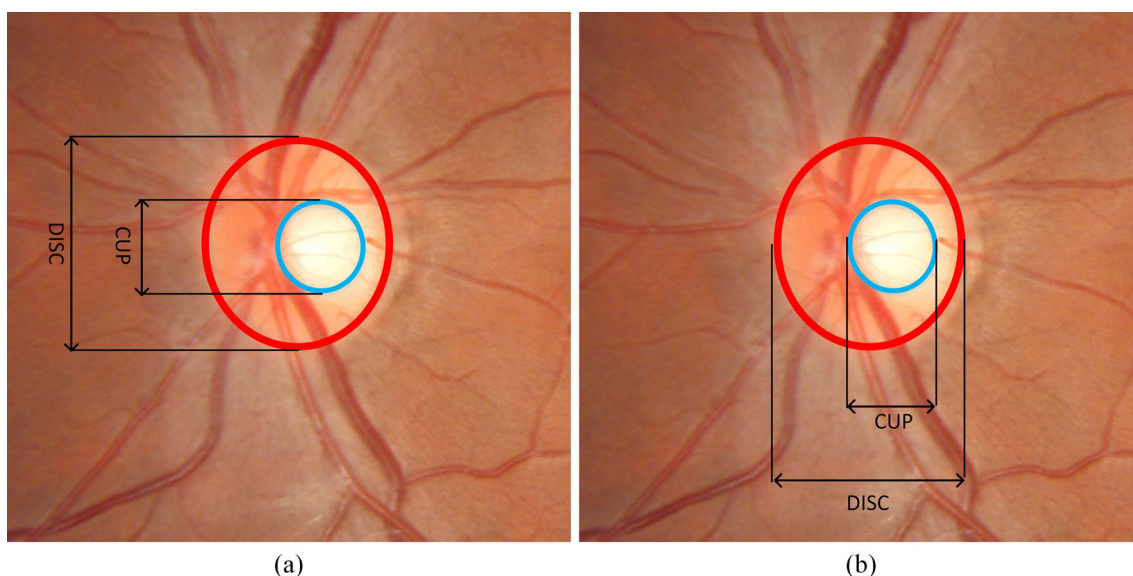

Fig. 7 Measurement of vertical CDR and horizontal CDR. (**a**) Measurement of vertical CDR. (**b**) Measurement of horizontal CDR

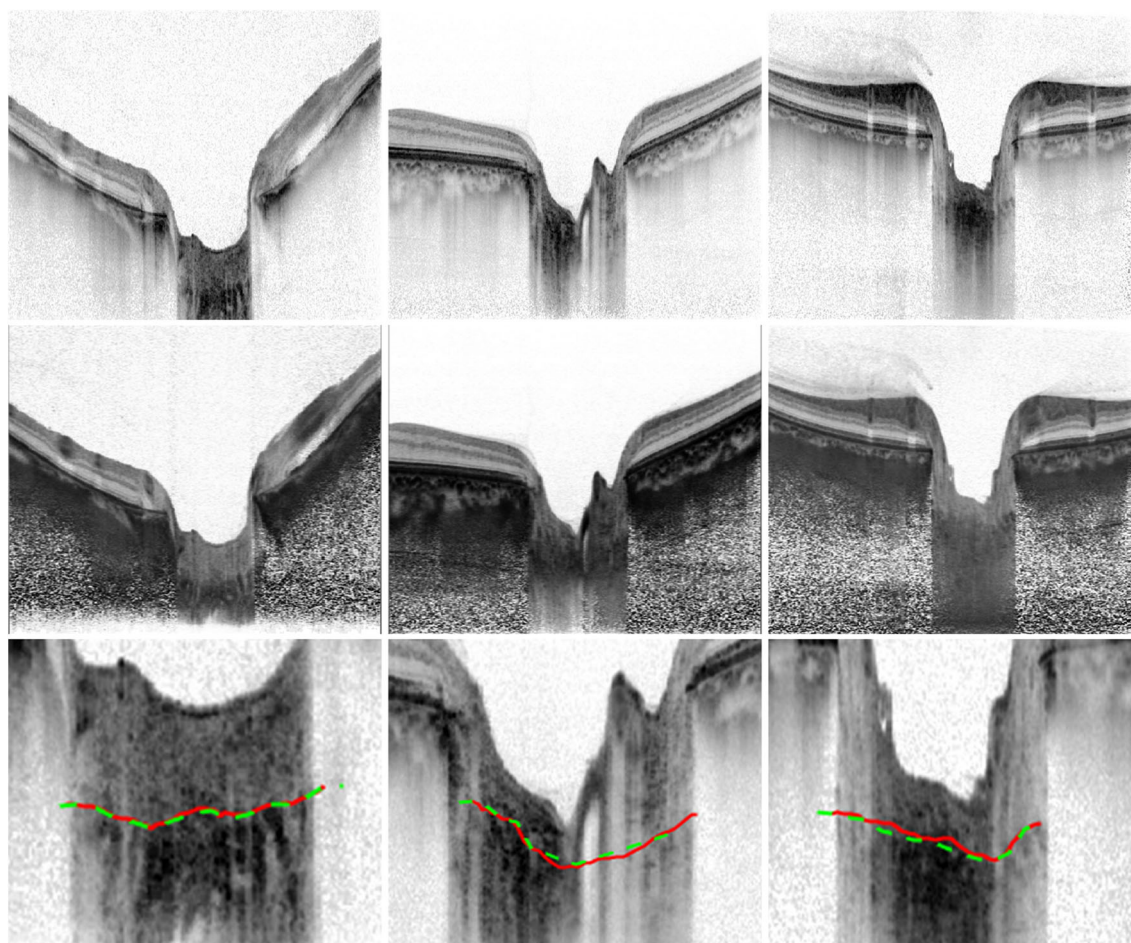**Table 1** Results of anterior lamina cribrosa segmentation

Method	Failure Ratio 0(%)	Failure Ratio 1(%)	Failure Ratio 2(%)
NLSC [14]	73.7	16.1	10.2
Method in [13]	76.5	17.6	5.9
The proposed method	78.1	16.2	5.7

Experiments and results

The proposed method for glaucoma screening was experimentally validated with a clinical dataset consisting of 12 glaucoma cases and 20 normal eye cases. Each eye has an EDI-OCT B-scan selected from all B-scans and a color fundus image. And an additional dataset with 46 EDI-OCT B-scans was used to train the residual U-Net. We trained and tested our network on an NVIDIA Titan V GPU with CUDA v9.0 acceleration. The network consists of 200,000 trainable parameters in total and it is fast to train the network to the stage of convergence because of residual learning skills. The network tested on 32 OCT B-scans in the clinical dataset and each B-scan was processed in 17 ms with the given hardware configuration. All samples were acquired from the Second Xiangya Hospital of Central South University. EDI-OCT images were captured by Heidelberg's Spectralis SD-OCT from Germany and fundus images were captured by Topcon fundus camera. An expert manually labeled the ALCS at each B-scan to evaluate the performance of the ALCS segmentation. In our experiments, EDI-OCT B-scan images were converted into anti-color images.

We measured the distance between the segmented ALCS and the ground truth for the evaluation of the performance of

Fig. 8 Results of anterior lamina cribrosa surface segmentation. The first row shows anti-color B-scans, the second row shows compensated B-scans after shadow removal and adaptive compensation, and the third row (cropped B-scans) shows the ground truths (red solid lines) and results of our proposed method (green dashed lines)

Table 2 Comparison of different methods

Method	TP	TN	FP	FN	Acc (%)	Sen (%)	Spe (%)
Based on EDI-OCT	11	19	1	1	93.75	91.67	95.00
Based on fundus images	10	20	0	2	93.75	83.33	100
EDI-OCT + fundus images	11	20	0	1	**96.88**	**91.67**	**100**

the proposed ALCS segmentation algorithm. The failure ratios (ranges from 0 to 2) are exploited for quantitative analysis. Failure ratio 0 indicates that the mean distance is between zero and two pixels, while failure ratio 1 indicates that the mean distance is between three and five pixels and failure ratio 2 indicates that the mean distance is more than five pixels. Table 1 presents the results of the comparison of the method in [13], the NLSC method [14] and our proposed ALCS segmentation algorithm.

In our experiments, about 500–1500 pixels with possibility greater than 0.5 are predicted in every B-scan. We select the pixel with the highest possibility in each column of a B-scan as the ALCS pixel. In each B-scan, about 60–180 ALCS pixels were obtained and we compared them to the ground truths by calculating the distance from the segmented pixels to the reference pixels. Table 1 suggests that our proposed ALCS segmentation algorithm gets better performance compared to the NLSC method and method proposed in [13]. The sum of failure ratio 0 and 1 in our proposed method was 94.3%, while NLSC was 89.8% and the method in [13] was 94.1%. Figure 8 shows the results of ALCS segmentation. We

cropped EDI-OCT B-scan images (3rd row) and retained areas of the optic nerve head for a more distinct observation.

It shows that our proposed method obtains excellent segmentation results with high matching degrees. The predicted pixels are very close to the reference pixels in Fig. 8. With the help of adaptive compensation (2nd row), blood shadows are removed and contrast is enhanced in the ONH area. The boundary of ALCS in blood shadow area is distinct, while the boundary that is not affected by blood shadows becomes blurry in some B-scans (3rd column). To handle this dilemma, we stack up a B-scan and its compensated B-scan as the inputs of our residual network. The anti-color B-scan offers more boundary information in areas that are not affected by blood shadows, while the compensated B-scan offers a more distinct boundary in blood shadow areas. Residual U-Net learns boundary features from both two kinds of images to obtain robust segmentation results.

To the best of our knowledge, our study is the first to combine EDI-OCT images and fundus images for glaucoma screening. Combination of structural parameters and textural features extracted from EDI-OCT images and fundus images

Table 3 Raw values of all features

Features	Glaucoma group	Normal group	Glaucoma sample (false negative)	Glaucoma sample	Normal sample
Minimal ALCSD	106.438 ± 28.29	72.550 ± 31.743	106.543	85.405	43.022
Maximal ALCSD	131.007 ± 30.16	98.728 ± 27.944	125.581	110.905	81.889
Average ALCSD	119.345 ± 29.07	86.815 ± 28.632	115.788	99.113	70.176
Slope ratio	0.579 ± 0.313	0.556 ± 0.322	0.463	0.571	0.286
Horizontal ratio	0.421 ± 0.313	0.444 ± 0.322	0.537	0.429	0.714
BMO-MRW1	26.628 ± 15.394	37.884 ± 16.760	13.000	24.331	44.721
BMO-MRW2	19.954 ± 6.648	42.592 ± 13.234	16.279	18.682	44.295
Vertical CDR	0.549 ± 0.125	0.502 ± 0.115	0.696	0.498	0.351
Horizontal CDR	0.530 ± 0.084	0.389 ± 0.151	0.498	0.462	0.349
Entropy	2.967 ± 0.251	2.916 ± 0.129	3.074	2.981	3.042
Correlation	0.955 ± 0.021	0.995 ± 0.001	0.996	0.960	0.996
Homogeneity	0.878 ± 0.029	0.909 ± 0.012	0.925	0.893	0.896
Correntropy-R	−1.187 ± 0.597	0.712 ± 0.033	0.697	−1.408	0.717
Correntropy-G	−1.164 ± 0.658	0.698 ± 0.112	0.907	−1.307	0.486
Correntropy-B	−1.182 ± 0.614	0.710 ± 0.018	0.749	−1.299	0.678
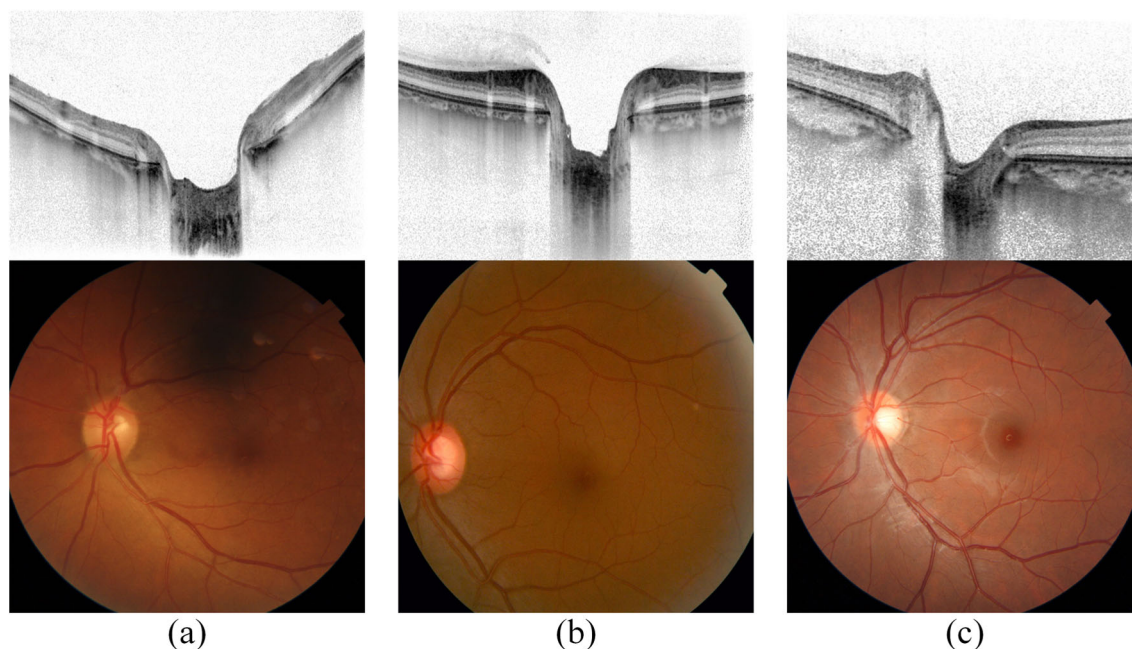
Fig. 9 B-scans and fundus images of three samples. (**a**) The wrongly classified sample. (**b**) Glaucoma sample. (**c**) Normal sample

was proven by experiments to be effective. Fusing multimodal features of EDI-OCT images and fundus images improved the performance of glaucoma screening. We used leave-one-out cross-validation to test the performance and stability of the proposed method for glaucoma screening. Results of the proposed method are shown in Table 2.

Among the total 32 samples, 11 of the 12 glaucoma samples were correctly predicted, and all normal samples were predicted to be normal eyes. Only one glaucoma sample was classified wrongly as a normal eye. Our proposed method showed excellent performance. We compared our method to the methods based on EDI-OCT images and based on fundus images. The method based on EDI-OCT images only used features extracted from EDI-OCT images, while method based on fundus images only used features extracted from fundus images. Table 2 shows a comparison of different methods. Our proposed method gets the best results with 96.88% accuracy, 91.67% sensitivity, and 100% specificity.

Table 3 lists the raw values of all features. It shows the mean and standard deviation in glaucoma group and normal group and all feature values of three samples (the wrongly classified sample, a glaucoma sample, and a normal sample) are also provided for a more distinct comparison. Note that

correntropy values in red, green and blue channels are averaged in each channel in Table 3. In Fig. 9, we present B-scans and fundus images of three samples for a more clear observation of differences between different samples. The wrongly classified sample is a glaucoma sample. It is observed in Table 3 that most clinical parameters (e.g., ALCSD, BMO-MRW, and CDR) indicate the sample may be a glaucoma sample rather than a normal sample while it is opposite when we take most textural features (e.g., correlation, homogeneity, and correntropy) into consideration, which confuses the classifier and leads to the misclassification.

We used TLBP method to obtain information of deformation of lamina cribrosa by calculating ratios of different templates to reduce the influence of lamina cribrosa holes and speckle noises. Table 4 shows the performances of different methods with TLBP or LBP. Our improved TLBP can reduce dimensions of features effectively and improve the performance of glaucoma screening. We obtained 96.88% accuracy and 91.67% sensitivity using our proposed method with TLBP, while 90.63% accuracy and 83.33% sensitivity were obtained with LBP. Besides, we use ALCD, BMO-MRW, and deformation of lamina cribrosa with TLBP or LBP in EDI-OCT for glaucoma screening. Results indicate that TLBP has

Table 4 Results of different methods with TLBP or LBP

Method	Accuracy(%)	Sensitivity(%)	Specificity(%)	AUC
Based on EDI-OCT with LBP	78.13	66.67	85	0.86
Based on EDI-OCT with TLBP	93.75	91.67	95	0.98
Proposed method with LBP	90.63	83.33	95	0.98
Proposed method with TLBP	**96.88**	**91.67**	**100**	**0.99**

better performance of extracting features of deformation of lamina cribrosa than LBP. We obtained 93.75% accuracy and 91.67% sensitivity using the method based on EDI-OCT images with TLBP and 78.13% accuracy and 66.67% sensitivity using the method based on EDI-OCT with LBP. Table 4 shows the comparison of the AUC of the aforementioned four methods respectively in Table 4. Higher performances are obtained using methods based on TLBP in comparison to methods based on LBP. In extracted LBP features, information of lamina cribrosa holes and speckle noises is also involved. That information is not beneficial for glaucoma screening. Template process in TLBP is designed to handle this problem and get exceptional results. Our proposed method with TLBP shows 6.9% improvement, while a 20% improvement is shown when we compare method based on EDI-OCT with TLBP and method based on EDI-OCT with LBP. It also indicates that the combination of EDI-OCT and fundus images reduces the effects of unnecessary information and increases robustness.

Conclusion

We propose a method for glaucoma screening combining EDI-OCT images and fundus images. In EDI-OCT images, region-aware strategy and U-Net are used to predict the possibility of pixels belonging to ALCS. Structural parameters are extracted from EDI-OCT images after ALCS segmentation. The optic disc boundary is detected in fundus images based on brightness reduction and sigmoid function and the optic cup is segmented by brightness compensation and threshold. CDR and textural features are extracted from fundus images. Our experiments show that combining multimodal features has given better results than using features from one kind of image.

The proposed method is primary research in combining multimodal features for glaucoma screening in EDI-OCT and color fundus images. It shows potential for early glaucoma screening by combining EDI-OCT and fundus images. In the future, we will collect more valid images and use more information in EDI-OCT images and fundus images like lamina cribrosa thickness for diagnosing glaucoma in the early stage.

Compliance with ethical standards

Ethical approval   All procedures performed in studies involving human participants were in accordance with the ethical standards of the institutional review board and with the 1964 Helsinki declaration and its later amendments or comparable ethical standards.

Conflict of interest   The authors declare that they have no conflict of interest.

References

1. Bourne, R. R., Stevens, G. A., White, R. A. et al., Causes of vision loss worldwide, 1990-2010: A systematic analysis. *Lancet Global Health.* 1(6):e339–e349, 2013. https://doi.org/10.1016/s2214-109x(13)70113-x.
2. Stevens, G. A., White, R. A., Flaxman, S. R. et al., Global prevalence of vision impairment and blindness: Magnitude and temporal trends, 1990-2010. *Ophthalmology.* 120(12):2377–2384, 2013. https://doi.org/10.1016/j.ophtha.2013.05.025.
3. Tham, Y. C., Li, X., Wong, T. Y. et al., Global prevalence of glaucoma and projections of glaucoma burden through 2040: A systematic review and meta-analysis. *Ophthalmology.* 121(11):2081, 2014. https://doi.org/10.1016/j.ophtha.2014.05.013.
4. Quigley, H. A., and Broman, A. T., The number of people with glaucoma worldwide in 2010 and 2020. *British journal of ophthalmology.* 90(3):262–267, 2006. https://doi.org/10.1136/bjo.2005.081224.
5. Chen, Z. L., Mo, Y. F., Ouyang, P. B. et al., Retinal vessel optical coherence tomography images for Anemia screening. *Medical & Biological Engineering & Computing.*, 2018. https://doi.org/10.1007/s11517-018-1927-8.
6. Chen, Z. L., Li, D. B., Shen, H. L. et al., Automated retinal layer segmentation in OCT images of age-related macular degeneration. *IET Image Processing.*, 2019. https://doi.org/10.1049/iet-ipr.2018.5304.
7. Tian, H., Li, L., and Song, F., Study on the deformations of the lamina cribrosa during glaucoma. *Acta Biomaterialia.* 55:340–348, 2017. https://doi.org/10.1016/j.actbio.2017.03.028.
8. Chien, J. L., Ghassibi, M. P., Mahadeshwar, P. et al., A novel method for assessing Lamina Cribrosa structure ex vivo using anterior segment enhanced depth imaging optical coherence tomography. *Journal of Glaucoma.* 26(7):626–632, 2017. https://doi.org/10.1097/IJG.0000000000000685.
9. Kiumehr, S., Park, S. C., Dorairaj, S. et al., In vivo evaluation of focal lamina cribrosa defects in glaucoma. *Archives of ophthalmology.* 130(5):552–559, 2012. https://doi.org/10.1001/archopthalmol.2011.1309.
10. Park, H. Y., and Park, C. K., Diagnostic capability of lamina cribrosa thickness by enhanced depth imaging and factors affecting thickness in patients with glaucoma. *Ophthalmology.* 120(4):745–752, 2013. https://doi.org/10.1016/j.ophtha.2012.09.051.
11. Kim, Y. W., Kim, D. W., Jeoung, J. W. et al., Peripheral lamina cribrosa depth in primary open-angle glaucoma: A swept-source optical coherence tomography study of lamina cribrosa. *Eye.* 29(10):1368–1374, 2015. https://doi.org/10.1038/eye.2015.162.
12. Sawada, Y., Hangai, M., Murata, K. et al., Lamina Cribrosa depth variation measured by spectral-domain optical coherence tomography within and between four glaucomatous optic disc phenotypes. *Investigative Ophthalmology & Visual Science.* 56(10):5777–5784, 2015. https://doi.org/10.1167/iovs.14-15942.
13. Chen, Z. L., Peng, P., Zou, B. J. et al., Automatic anterior Lamina Cribrosa surface depth measurement based on active contour and energy constraint. *Journal of Computer Science and Technology.* 32(6):1214–1221, 2017. https://doi.org/10.1007/s11390-017-1795-y.
14. Belghith, A., Bowd, C., Medeiros, F. A., et al., Automated segmentation of anterior lamina cribrosa surface: How the lamina cribrosa responds to intraocular pressure change in glaucoma eyes? 2015 12th IEEE International Symposium on Biomedical Imaging (ISBI), 2015. https://doi.org/10.1109/ISBI.2015.7163854.

15. Haleem, M. S., Han, L., Hemert, J. et al., A novel adaptive deformable model for automated optic disc and cup segmentation to aid Glaucoma diagnosis. *Journal of Medical Systems.* 42(20), 2018. https://doi.org/10.1007/s10916-017-0859-4.

16. Noronha, K. P., Acharya, U., Nayak, K. P. et al., Automated classification of glaucoma stages using higher order cumulant features. *Biomedical Signal Processing and Control.* 10:174–183, 2014. https://doi.org/10.1016/j.bspc.2013.11.006.

17. Khalil, T., Akram, M. U., Khalid, S. et al., Improved automated detection of glaucoma from fundus image using hybrid structural and textural features. *IET Image Processing.* 11(9):693–700, 2017. https://doi.org/10.1049/iet-ipr.2016.0812.

18. Issac, A., Sarathi, M. P., and Dutta, M. K., An adaptive threshold based image processing technique for improved glaucoma detection and classification. *Computer Methods and Programs in Biomedicine.* 122(2):229–244, 2015. https://doi.org/10.1016/j.cmpb.2015.08.002.

19. Maheshwari, S., Pachori, R. B., and Acharya, U. R., Automated screening of glaucoma using empirical wavelet transform and correntropy features extracted from fundus images. *IEEE Journal of Biomedical and Health Informatics.* 21(3):803–813, 2017. https://doi.org/10.1109/JBHI.2016.2544961.

20. Soltani, A., Battikh, T., Jabri, I. et al., A new expert system based on fuzzy logic and image processing algorithms for early glaucoma screening. *Biomedical Signal Processing & Control.* 40:366–377, 2018. https://doi.org/10.1016/j.bspc.2017.10.009.

21. Soorya, M., Issac, A., and Dutta, M. K., An automated and robust image processing algorithm for glaucoma screening from fundus images using novel blood vessel tracking and bend point detection. *International Journal of Medical Informatics.* 110:52–70, 2018. https://doi.org/10.1016/j.ijmedinf.2017.11.015.

22. Raghavendra, U., Fujita, H., Bhandary, S. V. et al., Deep convolution neural network for accurate diagnosis of Glaucoma using digital fundus images. *Information Sciences.* 441:41–49, 2018. https://doi.org/10.1016/j.ins.2018.01.051.

23. Niwas, S. I., Lin, W., Bai, X. et al., Automated anterior segment OCT image analysis for angle closure Glaucoma mechanisms classification. *Computer Methods & Programs in Biomedicine.* 130:65–75, 2016. https://doi.org/10.1016/j.cmpb.2016.03.018.

24. Gopinath, K., Sivaswamy, J., Mansoori, T., Automatic glaucoma assessment from angio-OCT images. 2016 IEEE 13th International Symposium on Biomedical Imaging (ISBI), 2016. https://doi.org/10.1109/ISBI.2016.7493242.

25. Zhou, Z.H., Feng, J., Deep Forest: Towards An Alternative to Deep Neural Networks. 2017 26th International Joint Conference on Artificial Intelligence (IJCAI), 2017. https://doi.org/10.24963/ijcai.2017/497.

26. Ronneberger, O., Fischer, P., Brox, T., U-net: Convolutional networks for biomedical image segmentation. 2015 18th International Conference on Medical Image Computing and Computer-Assisted Intervention (MICCAI), 2015. https://doi.org/10.1007/978-3-319-24574-4_28.

27. Drozdzal, M., Vorontsov, E., Chartrand, G., et al., The importance of skip connections in biomedical image segmentation. 2016 2nd Workshop on Deep Learning and Data Labeling for Medical Applications (DLMIA), 2016. https://doi.org/10.1007/978-3-319-46976-8_19.

28. He, K., Zhang, X., Ren, S., et al., Deep residual learning for image recognition. 2016 29th IEEE Conference on Computer Vision and Pattern Recognition (CVPR), 2016. https://doi.org/10.1109/CVPR.2016.90.

29. Mari, J. M., Strouthidis, N. G., Park, S. C. et al., Enhancement of lamina cribrosa visibility in optical coherence tomography images using adaptive compensation. *Investigative Ophthalmology and Visual Science.* 54(3):2238–2247, 2013. https://doi.org/10.1167/iovs.12-11327.

30. Girard, M. J., Tun, T. A., Husain, R. et al., Lamina cribrosa visibility using optical coherence tomography: Comparison of devices and effects of image enhancement techniques. *Investigative Ophthalmology and Visual Science.* 56(2):865–874, 2015. https://doi.org/10.1167/iovs.14-14903.

31. Krizhevsky, A., Sutskever, I., Hinton, G., ImageNet Classification with Deep Convolutional Neural Networks. 2012 25th International Conference on Neural Information Processing Systems (NIPS), 2012. https://doi.org/10.1145/3065386.

32. Ojala, T., Pietikainen, M., and Harwood, D., A comparative study of texture measures with classification based on featured distributions. *Pattern Recognition.* 29(1):51–59, 1996. https://doi.org/10.1016/0031-3203(95)00067-4.

33. Rhodes, L. A., Huisingh, C. E., Quinn, A. E. et al., Comparison of Bruch's membrane opening-minimum rim width among those with Normal ocular health by race. *American Journal of Ophthalmology.* 174:113–118, 2017. https://doi.org/10.1016/j.ajo.2016.10.022.

34. Nannini, D. R., Kim, H., Fan, F. et al., Genetic risk score is associated with vertical cup-to-disc ratio and improves prediction of primary open-angle Glaucoma in Latinos. *Ophthalmology.* 125(6):815–821, 2018. https://doi.org/10.1016/j.ophtha.2017.12.014.

35. Eleyan, A., Demirel, H., Co-occurrence based statistical approach for face recognition. 2009 24th IEEE International Symposium on Computer and Information Sciences (ISCIS), 2009. https://doi.org/10.1109/ISCIS.2009.5291895.

36. Xian, G. M., An identification method of malignant and benign liver tumors from ultrasonography based on GLCM texture features and fuzzy SVM. *Expert Systems with Applications.* 37(10):6737–6741, 2010. https://doi.org/10.1016/j.eswa.2010.02.067.

37. Gunduz, A., and Principe, J. C., Correntropy as a novel measure for nonlinearity tests. *Signal Processing.* 89(1):14–23, 2009. https://doi.org/10.1016/j.sigpro.2008.07.005.

38. Gilles, J., Empirical wavelet transform. *IEEE Transactions on Signal Processing.* 61(16):3999–4010, 2013. https://doi.org/10.1109/TSP.2013.2265222.